RSC Advances

PAPER

View Article Online
View Journal | View Issue

Cite this: *RSC Adv.*, 2023, **13**, 5081

Kinetic study of polydopamine sphere synthesis using TRIS: relationship between synthesis conditions and final properties

Juan Carlos García-Mayorga,[a] Haret-Codratian Rosu,[a] Alma Berenice Jasso-Salcedo[b] and Vladimir Alonso Escobar-Barrios *[a]

The synthesis and characterization of polydopamine (PDA) using dopamine (DA) as the monomer and (hydroxymethyl)aminomethane (TRIS) as the oxidant is studied. The effect of temperature and TRIS concentration on the kinetics of dopamine polymerization is evaluated, and the kinetic parameters are also calculated. Three TRIS concentrations are used to assess their effect on DA polymerization kinetics. The reaction at 1.5 mmol of TRIS shows a sustained increase of the rate constant with temperature from 2.38×10^{-4} to 5.10×10^{-4} when the temperature is increased from 25 to 55 °C; however, not all reactions follow an Arrhenius law. In addition, the correlation between the synthesis parameters and morphological, structural, and thermal properties of polydopamine is established. The morphology of the PDA particles is evaluated by Scanning Electron Microscopy (SEM), the relationships between the diameter, distribution size, and the rate constant. Thermal characterization by Differential Scanning Calorimetry (DSC) shows an endothermic transition around 130 °C associated with the melting of PDA's regular structure. It is supported by structural studies, such as infrared and Raman spectroscopy and X-ray Diffraction (XRD), by observing a broad peak at 23.1° (2θ) that fits with a graphitic-like structure of PDA.

Received 21st October 2022
Accepted 27th January 2023

DOI: 10.1039/d2ra06669f

rsc.li/rsc-advances

1. Introduction

Melanin is a polyphenolic material widely found in all living organisms, from bacteria to mammals. Melanin is found in animals' skin, hair, feathers, scales, and some neural tissues, like the cochlea, retina, and substantia nigra.[1,2] There are two main types of melanin, the black or brown insoluble eumelanin, found in human black hair and the retina; such eumelanin contains nitrogen and has a high molecular weight compared with pheomelanin, a different kind, which contains sulfur in its structure.[2] Eumelanin has a vital function in providing pigmentation and protecting the skin from phototoxic events due to sunlight irradiance. Melanin has antioxidant and free-radical scavenging behavior, broadband UV-visible absorption, photosensitization, metal ion chelation, and antimicrobial activity.[3] These features make it very interesting to study the possibility of using melanin as an active material for technological applications, such as molecular electronics and photovoltaic devices, since it is considered as an organic semiconductor.[4] In recent years, the synthetic melanin denominated as polydopamine (PDA) has taken much attention in the field of biomedicine,[5] electronics,[6] bioelectronics,[7] environmental remediation,[8] and photocatalysis.[9] PDA is a material that has a similar chemical structure to eumelanin and easily synthesized. One of its most remarkable applications is the remediation of contaminated water, where PDA is used as part of a photocatalyst to increase its photoactivity[9–11] at the same time, it has been used for surface modification due to its excellent adhesion properties at almost all surfaces caused by its similar structure to the essential adhesive component of mussel protein (presence of amine, imine, and catechol groups),[12,13] hydrogen generation,[14] remotion of herbicides,[15] sensors for colorimetry or glucose,[16,17] photothermal therapy to treat cancer,[18] and for drug encapsulation and release.[19–22] The synthesis and versatility of PDA processing allow achieving a diverse variety of shapes ranging from hollow or solid spheres or core–shell particles to thin films; it can even be used to decorate other particles.[7,23]

Additionally, thermodynamic and kinetic PDA synthesis studies are critical to establishing parameters like reaction order (n), pre-exponential factor (A), and activation energy (E_a). Such parameters are essential for polymerization control, affecting the material's final properties, and are critical to the technological use of the PDA. In this context, M. Salomäki *et al.*[24] did a thermodynamic study of dopamine oxidation and cyclization dependence on pH and oxidants like transition-

[a]*Advanced Materials Department, Instituto Potosino de Investigación Científica y Tecnológica A.C., Camino a la Presa San José, Lomas 4a Sección, San Luis Potosí, SLP, 78216, Mexico. E-mail: vladimir.escobar@ipicyt.edu.mx*

[b]*Departamento de Biociencias y Agrotecnología, Centro de Investigación en Química Aplicada, Blvd. Enrique Reyna Hermosillo No. 140, Saltillo, Coahuila, 25294, Mexico*

metal ions mainly focused on the early stages of the process. The authors proposed a general mechanism to understand the involved species during PDA polymerization and concluded that the most critical parameter for the process is the pK value. In the same way, the use of tuning radicals to control the size of PDA nanoparticles is reported by X. Wang *et al.*[25] In the latter study, the authors concluded that the polymerization could be inhibited or terminated from the free radical scavengers, while the stable radicals catalyzed the formation of PDA seeds. A comparable study was carried out by M. Wu *et al.*[26] who synthesized PDA through sodium hydroxide and developed a model about relationships between particle size, the molar ratio of DA, and oxidizing agent to control the particle diameter and distribution.

In addition, V. Ball *et al.*[27] studied the film deposition kinetics influenced by pH, DA concentration, and their effect on thickness, morphology, roughness, and surface energy expressing the relationship between maximal thickness and kinetic constant to obtain thickness higher than 45 nm.

In summary, controlling the PDA polymerization reaction is essential since it determines its yield, particle size, and properties like photothermal effect, UV protection, and free radical scavenging activity.[26,28] So far, the studies regarding the kinetics of PDA synthesis are few. One of the methods to have higher control over the synthesis of spheric PDA particles is the TRIS, which allows for obtaining small particles[29] as well as the formation of films where TRIS lets to obtain maximal thickness in the deposition of PDA films;[30] all of this in comparison with other buffers or alkalis like sodium hydroxide,[31] sodium bicarbonate,[32] ammonia,[33] and phosphate solution.[34] Nonetheless, relevant kinetics parameters like n, A, and E_a have not been provided regarding the synthesis of PDA spheres through TRIS. In this work, the aforementioned kinetic parameters are determined, and their relationship with the structure and properties of PDA is established.

2. Experimental

2.1 Materials

Dopamine hydrochloride (98%) and tris(hydroxymethyl)aminomethane (named TRIS, ≥99.8%) were purchased from Sigma Aldrich. All the chemicals were used as they were received, *i.e.*, without further purification. The solutions were prepared with deionized water (18.2 MΩ cm).

2.2 Synthesis

Briefly, 300 mg of dopamine hydrochloride (DA) was dissolved in a ball flask with 150 ml of deionized water (13 mM). The solution was stirred using a magnetic bar; meanwhile, three different quantities, 1.5 (pH = 8.50 at 25 °C), 4.5 (pH = 8.98 at 25 °C), and 7.5 (pH = 9.50 at 25 °C) Millimole (mmol) of TRIS, were added. The study was carried out at 25, 40, and 55 °C for every TRIS concentration. After 24 hours, the solution was centrifuged at 6000 rpm for 20 minutes and washed several times with deionized water to remove synthesis residues. The sediment was dried at 80 °C for 6 hours.

2.3 Kinetic analysis of the reaction

The polymerization reaction was monitored by UV-vis spectrometry in a quartz cell with a UV-vis-NIR spectrometer, CARY 5000 (Agilent, USA), in the range of 250 to 350 nm, and the maximum absorbance of DA was located at 280 nm. Then, aliquots were taken at 0, 1, 2.5, 5, 15, 45, 90, 180, 360, 600, and 1400 minutes; such aliquots were centrifugated to remove the presence of PDA. For an adequate measure of the absorbance, the aliquots were diluted with a factor of 20 with deionized water.

The UV-vis spectrum of PDA suspension was carried out once it was washed and dried to remove any trace of DA. Afterward, the PDA was re-suspended in water with a water/PDA ratio of 20. Spectrum was measured in a range from 200 to 500 nm.

2.4 Characterization of material

2.4.1 Morphology and particle size. The morphology of synthesized material was observed by Scanning Electron Microscopy in a Dual Beam Helios Nanolab 600 (FEI, USA) operated at 8.00 kV, a work distance of 5.0 mm, and a secondary electron detector; the samples were supported on carbon tape. The diameters of the particles were measured using the software ImageJ. The used micrographs were taken at 25 000× with measurements of 80 particles.

2.4.2 Thermal characterization. The thermal transitions were obtained by Differential Scanning Calorimetry (DSC) using a DSC Q200 (TA Instruments, USA) with a heating rate of 10 °C min^{-1} from −50 to 250 °C under a nitrogen atmosphere. The Thermogravimetric Analysis (TGA) was conducted using Q500 equipment (TA Instruments, USA) with a heating rate of 10 °C min^{-1} from room temperature to 700 °C under a nitrogen atmosphere.

2.4.3 Spectroscopic analyses. For such analyses, the Fourier Transform Infra-Red (FTIR) was obtained with a spectrophotometer Nicolet iS10 (Thermo Scientific, USA) using the ATR mode with 256 counts and 4 cm^{-1} resolution. At the same time, the Raman spectroscopy was carried out using a Micro Raman (Renishaw, UK), laser excitation at 532 nm, and a Raman shift range from 500 to 2000 cm^{-1}. All spectra were processed to establish the same baseline.

2.4.4 X-ray diffraction. XRD spectra were collected on an X-ray diffractometer D8 Advance (Bruker, USA) using Cu Kα radiation with a diffraction angular range from 5° to 60° in 2θ.

3. Results and discussion

3.1. PDA synthesis

The dopamine concentration at every condition was determined over time using UV-vis spectroscopy to evaluate its consumption kinetics. Fig. 1A shows the UV-vis spectra of dopamine solution at different reaction times with 1.5 mmol TRIS. The maximum peak is observed at 284 nm, which corresponds to the absorption by the aromatic ring in DA.[35] Regarding the spectra of the other reactions, they follow a similar trend; consequently, the spectrum at 1.5 mmol tris and 25 °C, is representative and for a clear observation, it is the only shown. It is worth mentioning

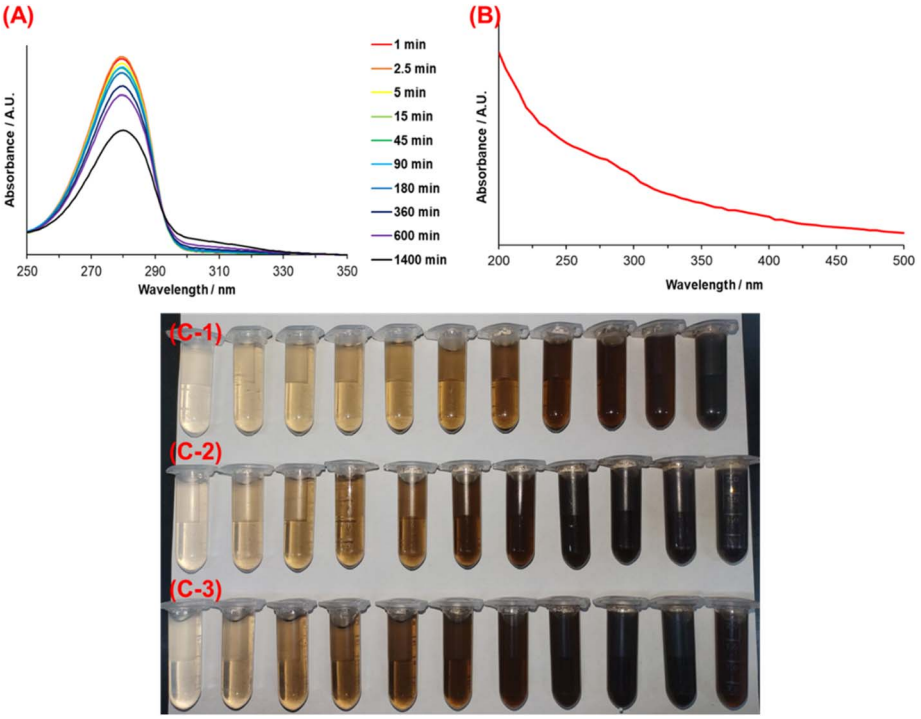

Fig. 1 (A) UV-vis spectra of the DA solution at different reaction times with 1.5 mmol of TRIS and 25 °C. (B) PDA spectrum in water solution. Reaction solution color change with 1.5 mmol TRIS, (C-1) at 25 °C, (C-2) at 40 °C, and (C-3) at 55 °C.

that PDA is a material with broadband monotonic absorption without a specific absorption wavelength. Thus, the spectrum of PDA is characterized by an exponential increase in absorbance toward the ultraviolet spectrum;[36] see Fig. 1B. Different points of view have been put forth to explain the origin of PDA's broadband absorption. For instance, according to R. Micillo *et al.*,[37] the broad spectra of PDA in UV-vis could be related to the 5,6-dihydroxyindole-based (DHI) oligomers of the material and its delocalized π – electrons systems. Nevertheless, another accepted theory argues that absorption in the ultraviolet region is due to dopamine transformation into dopachrome and dopaindol. At the same time, the presence of monomers (DA) in the PDA structure could generate absorption from visible to infrared wavelengths, which results from the subsequent self-polymerization process.[6,38]

Regarding the color of the solution, from Fig. 1(C-1)–(C-3), it is clear that it changed according to the reaction extent and depending on its initial reaction temperature. A color change from pale yellow to dark brown indicates the self-oxidation of DA to obtain PDA.

The exact polymerization mechanism of PDA is still under debate, mainly due to its insolubility in all solvents. Nonetheless, there have been significant attempts to explain it. According to the literature,[32,39] spontaneous auto-oxidation of dopamine accompanying intramolecular cyclization takes place, and alkali medium (pH ≥ 7.5) and dissolved oxygen are the key factors of the process.

Fig. 2A summarizes this process (illustration taken from ref. 40). Firstly, the catechol moiety of DA loses an e^- and H^+ to become dopamine semiquinone (DSQ), to oxidize again later, giving the dopamine quinone (DQ). Secondly, DQ undergoes intramolecular cyclization and oxidation to form leucodopaminechrome (LDC), which consequently gives rise to dopaminechrome (DC), which can re-arrange to DHI.

In addition, in analogy with the eumelanin, the hierarchical structure of PDA has been proposed, and three stages are established. The first stage is formed by oligomers of DA, DHI, or indolequinone (oxidized form of DHI, IDQ) species that could be covalently bounded by C–C in 2, 4, or 7 position for DHI and 2 or 5 position for DA, "covalent oxidative polymerization"; or they could be directly assembled by physical interactions (hydrogen bonds between oxidized species of catechol moieties), "physical self-assembly pathways", as it is shown in Fig. 2B.

In contrast, other investigations have indicated that during the self-oxidation of DA, species like pyrrole carboxylic acids or catechol-containing carboxylates can be developed due to the oxidative destruction of the phenyl ring of the indole structures. These can be found as part of the structure of PDA, mainly when L-DOPA is used as a precursor.[42] The second stage is built through stacking oligomers (trimers and tetramers) and non-covalent interactions like π–π interaction. In the last stage, aggregates are formed by weak non-covalent interactions between the structures.[40,43] Additionally, temperature accelerates such oxidation, which is why a darker solution for the highest temperature (55 °C) is observed earlier than the reactions carried out at 25 and 40 °C (Fig. 1C). Thus, the influence of temperature on the reaction rate is evident, and an Arrhenius-type behavior is expected.

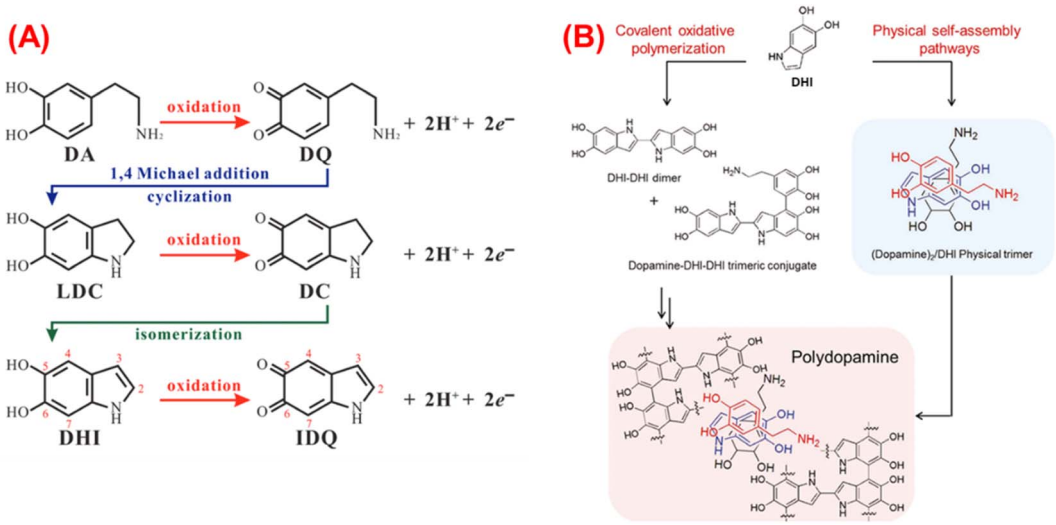

Fig. 2 (A) Chemical route of the DA auto-oxidation,[40] (B) PDA formation through the different oligomers.[41]

3.2 Polymerization kinetics

Fig. 3 shows the DA concentration profile over time for every synthesis condition. The mathematical model used to adjust the data exhibited an exponential decrease. Regarding the general expression, reagents → products, eqn (1) and (2) display the reaction of DA conversion to PDA and the rate law, respectively.

$$\mathrm{DA} \xrightarrow{\mathrm{pH} > 7.5} \mathrm{PDA} \tag{1}$$

$$-\frac{\mathrm{d}[\mathrm{DA}]}{\mathrm{d}t} = -r_{[\mathrm{DA}]} = k[\mathrm{DA}]^n \tag{2}$$

Applying natural logarithms to eqn (2), the mathematical equation corresponds to a linear equation (eqn (3)), where the slope corresponds to the reaction order n, and the intercept b corresponds to Ln(k), from which the rate constant can be obtained.

$$\mathrm{Ln}(-r_{[\mathrm{DA}]}) = n\mathrm{Ln}([\mathrm{DA}]) + \mathrm{Ln}(k) \tag{3}$$

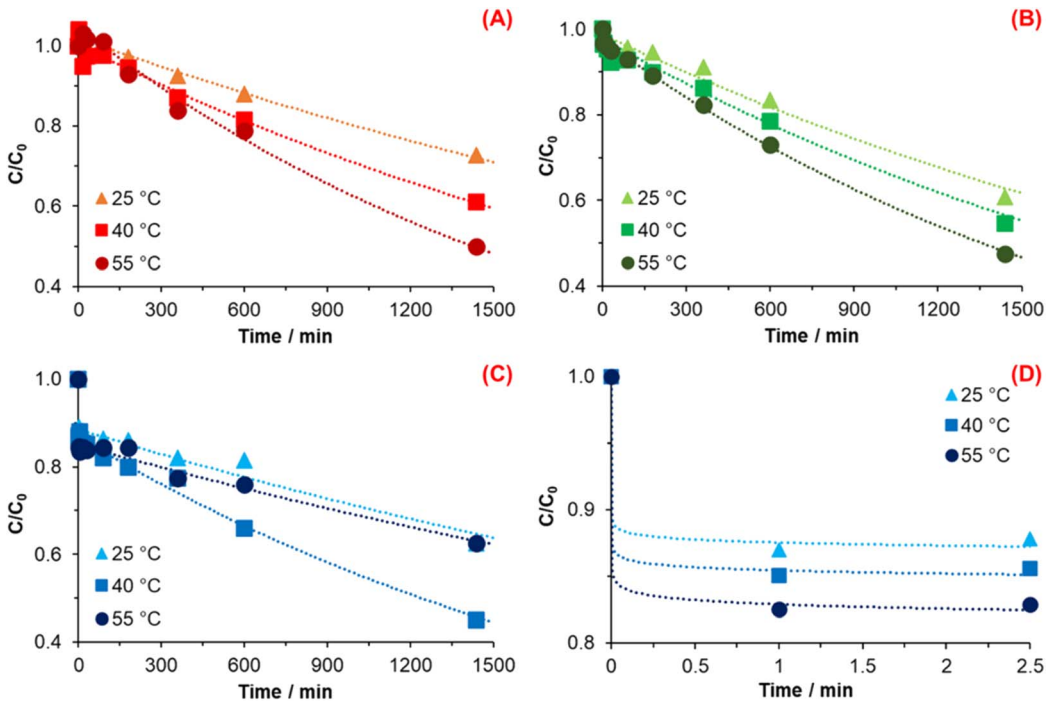

Fig. 3 Change of dopamine concentration against time and exponential decline fitting for (A) 1.5 mmol TRIS, (B) 4.5 mmol TRIS, (C) 7.5 mmol TRIS, and (D) zoom of the reaction onset at 7.5 mmol TRIS.

Table 1 summarizes the values of the rate constant and reaction order from each temperature and TRIS concentration used.

The synthesis of PDA with 1.5 mmol showed an increase in the reaction rate (Fig. 3A) as the temperature was increased, as was expected (Table 1). This behavior indicates that the reaction, under such conditions, follows typical behavior in terms of kinetics and the mechanism as proposed by Della Vecchia *et al.*[29] Chemical kinetics—specifically the theory of collisions—indicates that when temperature increases in a chemical reaction, molecules' kinetic energy also increases. Consequently, the molecules have more energy to react and form products due to more collisions caused by the temperature increase,[44] which exhibit an increment of 0.37 and 1.14 times when the temperature increase to 40 and 55 °C, respectively, concerning the rate constant at 25 °C.

The reaction order of the synthesis carried out with 1.5 mmol of TRIS was $n \sim 1$ for every temperature. It means that the reaction of PDA formation depends linearly on the DA concentration. In other words, the reaction order of PDA synthesis implies the exponential decrease of DA concentration as a function of time, while the reaction rate decrease linearly as a function of concentration.

Fig. 3B displays the relationship of DA concentration *vs.* time at 25, 40, and 50 °C with 4.5 mmol of TRIS; the calculated values of the reaction order and rate constant for every reaction temperature were $n \sim 1$ and $k = 2.53 \times 10^{-4}$, 3.28×10^{-4}, and 4.65×10^{-4} min^{-1}, respectively. In the same way, reactions carried out at 4.5 mmol TRIS show similar behavior concerning 1.5 mmol when the temperature increases; it represents an increment of the k as the temperature increase.

When the rate constants of 1.5 and 4.5 mmol TRIS are compared, a TRIS concentration effect can be noticed. TRIS molecule possesses three OH groups which are ionized when it is in solution; a higher concentration of OH^- ions means that the Michael addition is accelerated.[45] Michael's addition is an essential step in the DA auto-oxidation for the formation of DQ, where the catechol moiety of DA is oxidized, losing an e^- and H^+ with the participation of O_2. However, this increase in the k value derived from hydroxyl ions concentration is limited to 25 and 40 °C since 55 °C is smaller than the k calculated with 1.5 mmol at the same temperature (Table 1).

As mentioned by M. Wu *et al.*,[26] the synthesis of nanoparticles of PDA implies two stages. The first one is the formation of PDA seeds, which grow during the second stage. Variables like temperature, pH, oxidants, and concentration of DA during its polymerization affect both stages. Polymerization of DA is accelerated by a high initial concentration of OH^- ions.

Table 1 Reaction order and rate constants for every reaction condition

T/°C	$n_{1.5}$	$k_{1.5}$/min^{-1}	$n_{4.5}$	$k_{4.5}$/min^{-1}	$n_{7.5}$	$k_{7.5}$/min^{-1}
25	1.00	2.38×10^{-4}	0.98	2.53×10^{-4}	0.92	1.50×10^{-4}
40	0.97	3.26×10^{-4}	0.98	3.28×10^{-4}	0.98	3.97×10^{-4}
55	0.98	5.10×10^{-4}	1.00	4.65×10^{-4}	0.97	1.78×10^{-4}

In parallel to an increment in temperature, its effect leads to a higher nucleation rate of PDA particles and, thus, to forming more seeds.[29,46] However, DA as a precursor for the PDA synthesis is consumed rapidly, and when more nuclei are formed, DA becomes unavailable for the particle growth stage. We assume that due to a slower growth stage of PDA particles, the observed k at 55 °C with 4.5 mmol TRIS could be lower than k with 1.5 mmol TRIS at the same temperature.

Fig. 3C and D illustrate the change in DA concentration over time for reactions with 7.5 mmol TRIS. Fig. 3D displays the change in DA concentration at 0, 1, and 2.5 minutes where a sudden decrease in DA concentration is observed as the TRIS solution was added. This reduction conveys an increment in TRIS concentration and temperature, which is correlated with the formation of seeds during the first stage of DA polymerization.

In order to estimate the oxidized DA and consumed for PDA nuclei, Fig. 4 shows the percent decrease in DA at the first instant after TRIS addition for all concentrations and temperatures. As is exhibited, for the reaction with 1.5 mmol TRIS, there is no sudden consumption of DA in the nuclei formation stage at the measurement's first time. However, for reactions at 4.5 mmol TRIS, one can notice a reduction of 2% in the DA concentration at 25 °C, which increases to 3.4% for the reaction at 55 °C; likewise, at 7.5 mmol TRIS, the DA concentration reduces by 11.7, 13.5, and 15.8% for 25, 40 and 55 °C, respectively. As mentioned before, OH^- ions and temperature accelerate the DA oxidation, which promotes the formation of DQ, an essential step for the PDA seeds formation; from these results, it is also observed that an increment in TRIS concentration is more relevant for nuclei construction than an increment in temperature. At 25 °C, the consumption of DA was 0, 2.00, and 11.72% as the hydroxyl ions increased, an effect also observed for 40 and 55 °C, where the percentage of DA decrease was from 0 to 3.41 and 13.46%; and from 0.61 to 3.44 and 15.74%, respectively. In contrast to TRIS concentration, the lower effect of temperature could be explained as the dependence on dissolved oxygen, which is essential for the auto-oxidation of DA.[47]

From the results observed for DA polymerization with 7.5 mmol of TRIS was supposed that the reaction has two different rate constants. The first is associated with the sudden decrease of DA at the first moments of the reaction, and the

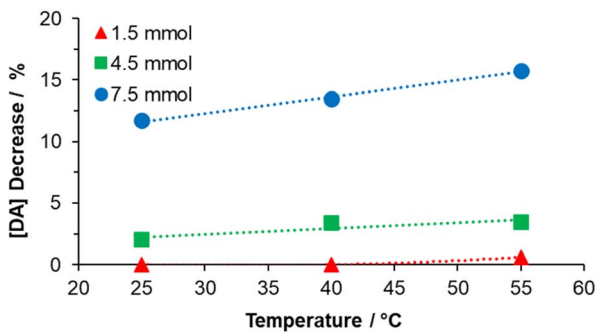

Fig. 4 Effect of the TRIS solution on DA consumption in the solution immediately after its addition (one minute after).

second is related to the subsequent decrease of DA. Due to the high-speed consumption of DA, it was not possible to determine the rate constant at the first moments. At the same time, the reaction order was assumed to be a superior order, which explains the decrease in DA concentration over time.

From the profiles obtained with 7.5 mmol TRIS shown in Fig. 3C, the second rate constant, the reaction rate at 55 °C, is lower than that at 40 °C and is similar to that of 25 °C. The computing values for reaction order and rate constants at 25, 40, and 55 °C were $n \sim 1$; and $k = 1.50 \times 10^{-4}$, 3.97×10^{-4}, and 1.78×10^{-4} min^{-1}, respectively. When the temperature rises to 40 °C, the rate constant increases 1.64 times in relationship with k at 25 °C, which corresponds with an Arrhenius behavior and an increment of OH^- concentration.

Nevertheless, the rate constant decreases when the temperature increases to 55 °C. According to ref. 25, the use of free radical scavengers (*i.e.*, edaravone) has an inhibition or termination effect during the DA polymerization, resulting in a decrement in particle size and yield. This effect occurs due to a reduction process promoted by edaravone during the oxidation of DA to DSQ species formation. It serves as an H-atoms donor to DSQ, which generates stable compounds. When the reaction is carried out at high temperatures, it implies the dissociation of water molecules, changing the concentration of H^+ and OH^- ions; in parallel, the generated species during DA oxidation with dissolved oxygen like H_2O_2 and $HO_2\cdot$ (Salomäki, M. *et al.*[24]) also could be a source of H^+. Herein, we assume that very high –OH ions concentrations (TRIS) affect the chemical kinetics of PDA polymerization, causing the inhibition/termination of the growth stage of PDA particles, which causes a lower k at 55 °C is obtained. In other words, when rate constants at 55 °C at different TRIS concentrations (Table 1) are compared, it is observed that reversibility in the DQ formation and inhibition/termination effects are more substantial when temperature and TRIS concentration increased, affecting the rate constant. Similar results were reported by X. Wang *et al.* where higher pH values (>9.55) gave lower yields.

According to chemical kinetics principles, most chemical rate constants increase as the temperature increases, and the Arrhenius equation (eqn (4)) expresses this relationship.

$$k = Ae^{-\frac{E_a}{RT}} \quad (4)$$

The Arrhenius parameters, activation energy (E_a), and pre-exponential factor (A) were calculated from the plot of Ln(k) against $1/T$ that gives a straight line ($y = mx + b$) where the slope (m) is $m = -E_a/R$, while $b = \mathrm{Ln}(A)$ provides the pre-exponential factor, see Table 2. The E_a is the minimum kinetic energy that reactants must have to generate products. Thus, 20.6 kJ mol^{-1} is the E_a computed for the reaction at 1.5 mmol while, for 4.5 mmol, it decreases to 16.48 kJ mol^{-1}. This effect means that a high pH (concentration of OH^-) reduces the activation energy—four-fifths compared to 1.5 mmol—needed to carry out the reaction of DA polymerization. In addition, the calculated E_a at 7.5 mmol TRIS, just for 25 and 40 °C, is 50.27 kJ mol^{-1}. High activation energy values imply a strong dependence of the rate constant on temperature, a result supported by the above-calculated rate constants. Moreover, in the case of 40 and 55 °C, the obtained $E_a = -45.5$ kJ mol^{-1} describes the rate decrease as the temperature increases.

Table 2 Activation energy and pre-exponential factor computed from rate constants

	1.5 mmol	4.5 mmol	7.5 mmol
E_a/kJ mol^{-1}	20.60	16.48	50.27
A/min^{-1}	0.94	0.19	96 374

Fig. 5 shows the plot E_a *vs.* Ln(A); as is observed, A for DA polymerization increases linearly with E_a. This relationship is explained by Brønsted acid sites (or active sites) in catalysts.[48,49] According to these works, an increase in active centers corresponds to a higher value of A; also, due to statistical and thermodynamic reasons, these active sites should be more numerous with decreasing energy. Additionally, they are less effective with lower energy. In other words, low energy in the active centers is accompanied by a high value of E_a.

Above all, this linear relationship between E_a and Ln(A) could be explained by DA polymerization in the growth stage. DA monomers react on the surface of previously formed PDA particles, where active sites like catechol moiety (acid site) and secondary amine (basic site) can affect the auto-oxidation and polymerization of DA.

3.3 Morphological analysis

Fig. 6 shows the micrographs for every PDA sample obtained by scanning electron microscopy and its corresponding particle diameter distribution (Table 3). The results for 1.5 TRIS concentration at 40 and 55 °C (Fig. 6B and C) display an average radius of 170.8 and 358.8 nm with broad particle distributions and standard deviations (SD) of 255.6 and 181.7, respectively. These materials, obtained at 40 and 55 °C, show a variety of particle sizes composed of separated and agglomerated particles, in contrast with the material obtained at 25 °C (Fig. 6A) that displays seemingly small regular fused particles forming

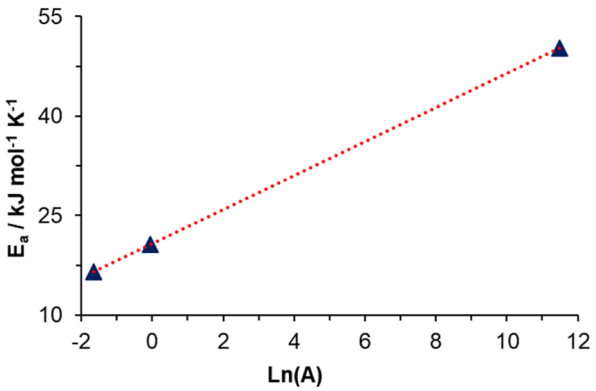

Fig. 5 E_a *vs.* Ln(A) in the range of temperatures of 25 to 55 °C.

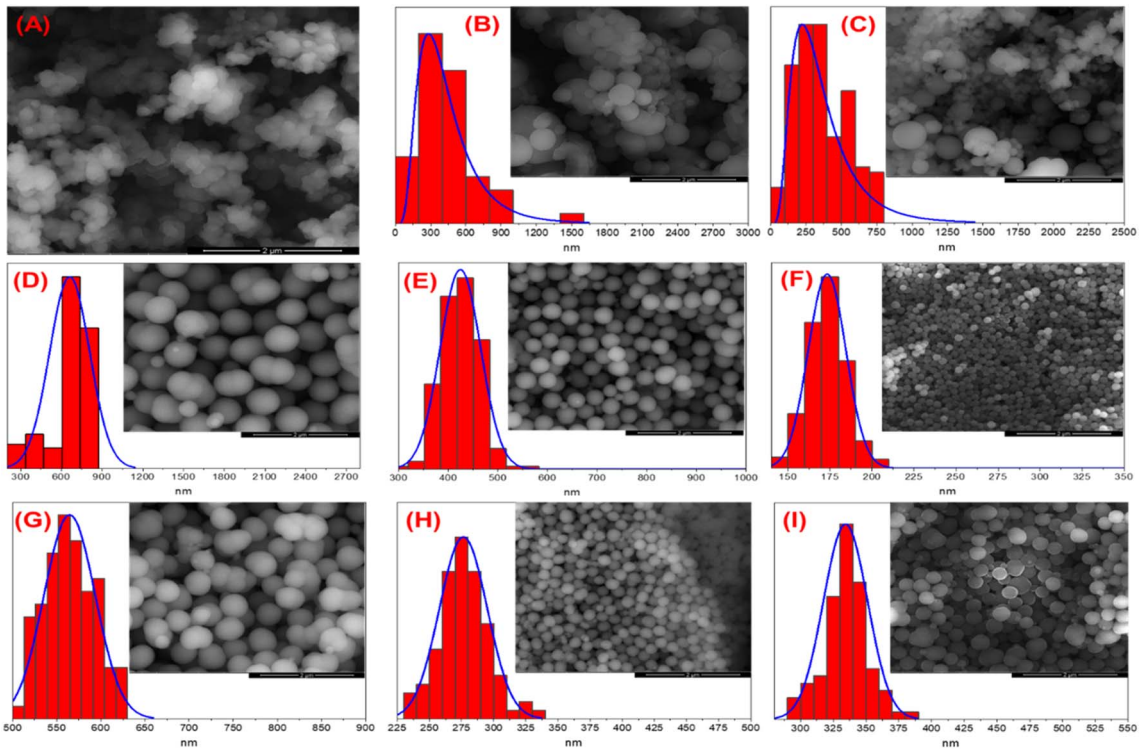

Fig. 6 Micrographics of PDA synthesized at different conditions and particle diameter distribution; (A) 1.5 mmol, 25 °C, (B) 1.5 mmol, 40 °C, (C) 1.5 mmol, 55 °C, (D) 4.5 mmol, 25 °C, (E) 4.5 mmol, 40 °C, (F) 4.5 mmol, 55 °C, (G) 7.5 mmol, 25 °C, (H) 7.5 mmol, 40 °C and, (I) 7.5 mmol, 55 °C. The bar represents 2 μm.

Table 3 Diameter and SD of particle size

Material		Diameter/nm	SD
1.5 mmol	25 °C	—	—
	40 °C	438.4	255.6
	55 °C	358.8	181.7
4.5 mmol	25 °C	661.2	148.0
	40 °C	424.6	40.9
	55 °C	173.3	11.3
7.5 mmol	25 °C	564.6	29.1
	40 °C	276.4	18.6
	55 °C	334.3	16.9

large agglomerates. Agglomerates observed at 25 °C could be formed by seeds that grow and fuse as the reaction advances. However, when the temperature increases, well-defined and bigger particles appear.

The Ostwald ripening process explains a wide distribution of diameter particles at 40 and 55 °C.[50] This process occurs when little particles are dissolved; the DA monomers from the surface of the smaller particles migrate to larger ones, resulting in bigger particles and wide distribution due to the higher surface energy of smaller particles; according to the Gibbs–Thompson relationship, these tend to dissolve.

The micrographs at 4.5 mmol TRIS (Fig. 6D–F for 25, 40, and 55 °C, respectively) show well-defined spherical particles with a narrow distribution (Table 3). A more spherical morphology is observed as a result of a higher concentration of TRIS than reactions at 1.5 mmol TRIS. Additionally, the temperature also affects the size distribution and average diameter.

Results from 7.5 mmol TRIS concentration at various temperatures (Fig. 6G–I) also show well-defined particles with average diameters of 564.6, 276.4, and 334.3 nm and SD of 29.1, 18.6, and 16.9 nm, respectively. In the same way, the effect of higher TRIS concentration gives better-defined particles. However, the diameter of PDA particles is not correlated with temperature since an increment from 25 to 40 °C represents a decrement from 564.6 to 276.4 nm; but when the temperature increases to 55 °C, the average size increases to 334 nm. In order to explain the change in particle size, the rate constant has a better fit. Although the temperature affects the rate constant, the inhibition/termination effect on PDA polymerization affects the rate constant and particle size, as mentioned before. In summary, the polymerization of PDA strongly depends on TRIS concentration and temperature; higher concentrations of TRIS encourage well-defined spherical particles and affect the particle size and distribution, an equally promoted effect by temperature from the rate constant.

3.4 Thermal analysis

Thermogravimetric analysis of DA (Fig. 7A) shows thermal stability up to 210 °C; after this point, dopamine degradation begins. Two main thermal stages are observed; the first is from 210 to 330 °C, where the degradation of catechol moiety is carried out, and the second is from 330 to 465 °C, associated

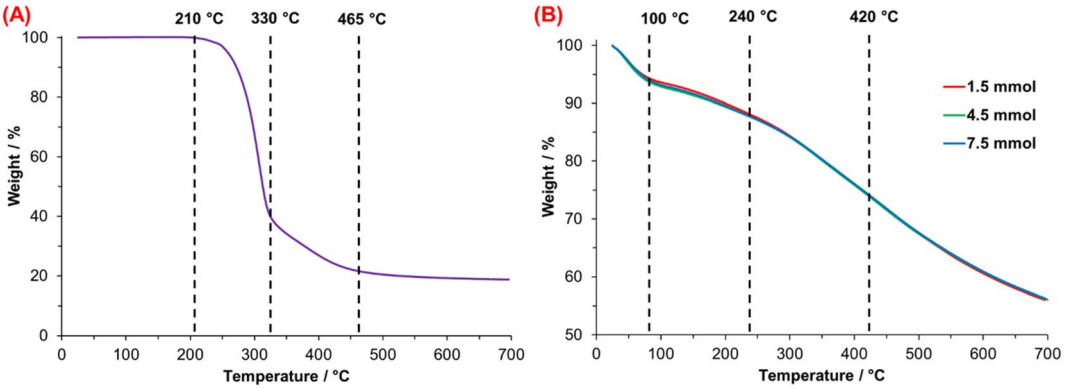

Fig. 7 Thermogravimetric analysis of (A) dopamine hydrochloride (DA·HCl) and (B) synthesized PDA at 25 °C.

with the decomposition of the alkyl spacer and the amine group.[51] The residue was 18.7% which corresponds to calcinated DA.

In the case of PDA, Fig. 7B shows the TGA thermograms of PDA synthesized with 1.5, 4.5, and 7.5 mmol TRIS. All the materials show similar and multistep weight loss associated with chemical heterogeneity. Four steps in the thermal degradation of PDA are identified; the first one is related to the evaporation of weakly bound water due to high PDA hygroscopicity,[52] observed from 25 to 100 °C. The second one—between 100 and 240 °C—corresponds to the release of intramolecular, strongly-bonded water.[53] The third step associated with the decomposition of aliphatic components[52] presented in PDA originated from DA molecules non-oxidized during the polymerization. Finally, with a final average mass retention of 56.2%, the last step from 420 to 700 °C matches with aromatic compounds like catechol or the *o*-benzoquinone moieties that decompose in this temperature range.[54]

Table 4 summarizes the loss in weight of PDA computed for each material at the final temperature of the four-step degradation process. The weight loss at 100 °C oscillates between 6.30 and 7.12%, with differences of 0.31%; this was the highest difference value of the four steps losses associated with the high material hygroscopicity. Molecular water trapped between PDA microstructure from the synthesis medium needs more heat to be released; the average weight loss of this process was 5.57%, with narrow differences (variation of 0.17%). The average weight loss of 25.8% at 420 °C is 0.19%, similar to the variation at 700 °C (0.13%). Low differences and similar behavior of PDAs after 240 °C could be associated with the similar chemical composition of PDA synthesized under different conditions.

The literature about natural and synthetic melanin postulates that these materials do not have a defined structure, considering them amorphous materials.[54–57] On the other hand, E. Coy *et al.*[58] have reported contradictory results for synthesized PDA characterized by Raman spectroscopy without any thermal treatment, which shows characteristics related to carbonized PDA particles; this material displays regular zones that indicate nanocrystalline graphite-like structure.[59] In addition, according to polymers science,[60,61] characteristic endothermic peaks observed by DSC are associated with the fusion of crystalline regions present in the microstructure of polymers.[62] The crystalline fraction can be computed by the quotient of the melting enthalpy (heat associated with the fusion process) measured and the melting enthalpy of the completely crystalline material.

The first authors that propose the relationship between the endothermic process of natural and synthetic melanin and a phase transition based on the granule nucleus organization were Simonovic B. *et al.*[63] The DSC thermograms of PDA are shown in Fig. 8. A broad endothermic peak with a maximum is

Table 4 Thermal characteristics of PDA analyzed by TGA and DSC

		Weight loss/%				DSC results	
Material		25–100 °C	100–240 °C	240–420 °C	420–700 °C	Melting peak/°C	Enthalpy/J g^{-1}
1.5 mmol	25 °C	6.42	12.13	26.04	43.92	125.0	304.5
	40 °C	6.82	12.34	25.60	43.66	124.5	340.9
	55 °C	6.39	12.00	25.79	43.93	137.2	346.6
4.5 mmol	25 °C	6.30	12.05	26.03	43.89	98.1	308.2
	40 °C	7.12	12.39	25.82	43.89	99.1	412.5
	55 °C	6.97	12.44	25.62	43.67	100.8	297.9
7.5 mmol	25 °C	6.42	12.13	26.04	43.92	139.2	307.5
	40 °C	6.39	12.00	25.79	43.93	123.9	338.9
	55 °C	6.82	12.34	25.60	43.66	145.7	280.2

observed between 98 and 146 °C; this first-order transition is linked with the melting process of PDA. As mentioned above, the chemical composition of PDA consists of layers (oligomers) composed of 3–4 units of mainly 5,6-dihydroxindole and DA molecules covalently bonded. Simultaneously, these layers interact by π–π systems, giving rise to ordered short-range regions. These arrangements, known in polymer science as lamellae crystals, suggest the presence of crystalline regions in PDA, which are destroyed by heating, explaining the transition observed by DSC.

Thermograms show the effect of synthesis conditions through the form—narrow or broad—of the endothermal peak (melting temperature) and melting enthalpy. Such thermograms indicate different melting temperatures due to crystallite imperfections and non-uniformity in their size. For instance, Yu, X. *et al.*[64] reported dark domains of graphite-like nanostructures with short-range (2–3 layers) and large-range (~40 layers) on calcinated PDA particles using High-Resolution Transmission Microscopy.

Fig. 8 illustrates the PDA thermograms synthesized with 1.5, 4.5, and 7.5 mmol TRIS at the three temperatures. Thermograms from synthesis at 4.5 mmol TRIS (Fig. 8B) show similar melting enthalpies compared with 1.5 and 7.5 mmol TRIS, but the melting points are lower (between 27 and 35 °C, Table 4). These results indicate that pH (TRIS concentration) and temperature have an essential effect on the conformation of PDA microstructure with an accentuated effect at 4.5 mmol TRIS concentration.

The associated enthalpy for each material is also listed in Table 4. It is worth mentioning that there are no data in the literature about melting enthalpy for crystalline PDA. Thus, it is not possible to calculate the crystalline fraction for these materials. However, if it is assumed that the PDA with the higher enthalpy value has the highest crystalline fraction (100%), which was obtained with 4.5 mmol TRIS at 40 °C, then 7.5 mmol TRIS at 55 °C produces the PDA with the lower crystalline fraction, 67.98%.

On the other hand, a minimum effect of TRIS concentration on the melting enthalpies for 1.5, 4.5, and 7.5 mmol at 25 °C is noticed. When the temperature increases to 40 and 55 °C, the effect of TRIS concentration is substantial; for instance, at 1.5 mmol, the temperature favors the formation of crystalline fractions in PDA, while the crystalline fractions at 40 °C are higher than those at 25 °C, at 4.5 and 7.5 mmol. But at such TRIS concentration and 55 °C, the crystalline fraction is reduced regarding that at lower temperatures. It is assumed that this effect relates to the chemical kinetics of PDA synthesis; at low TRIS concentration, the effect of temperature is directly proportional to the crystalline fraction.

On the contrary, this relationship changes when TRIS concentration increases to 7.5 mmol, which modifies the rate constant, see Fig. 9A. According to Yu, X. *et al.*, there are more stacking layers on the shell than in the inner of PDA particles, which could be affected by the inhibition/termination or Ostwald ripening process on the surface of particles during the growth stage.

A correlation between the endothermal transition and inner water molecules in the microstructure also can be established in the 100–240 °C range, where the melting of crystalline regions of PDA led to water molecules–from reaction media—to be released. Nonetheless, the enthalpy associated with this process is much lower than the associated melting enthalpy.[53,63]

Fig. 9B illustrates the correlation between the synthesis and melting temperature, where most crystalline regions disappear;

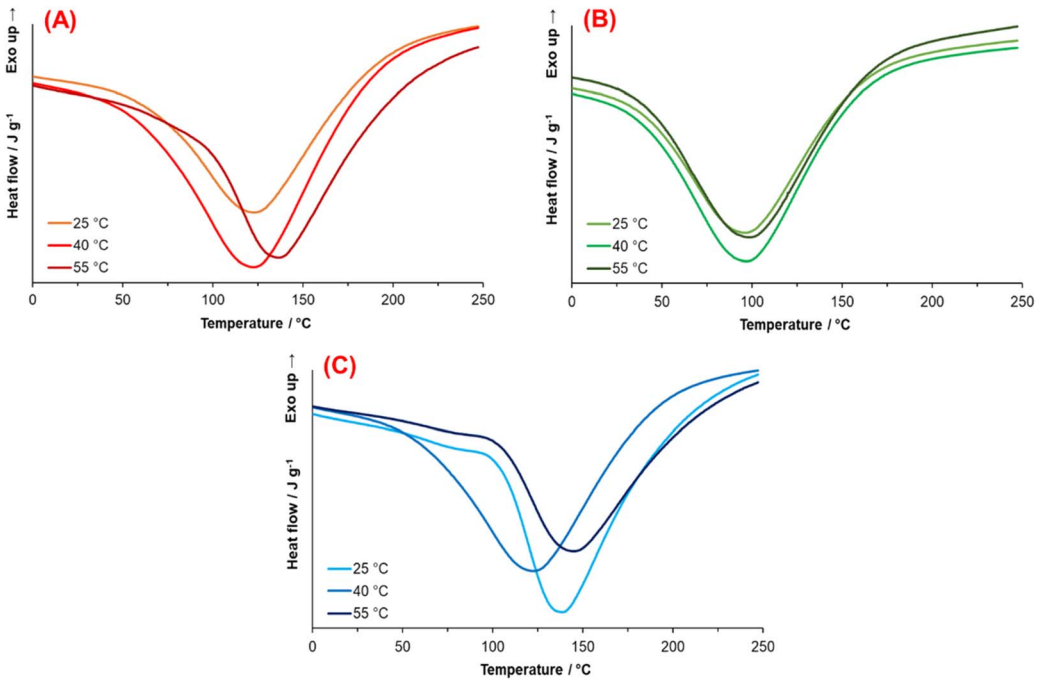

Fig. 8 Thermograms obtained from PDA synthesized at (A) 1.5 mmol, (B) 4.5 mmol, and (C) 7.5 mmol for each temperature.

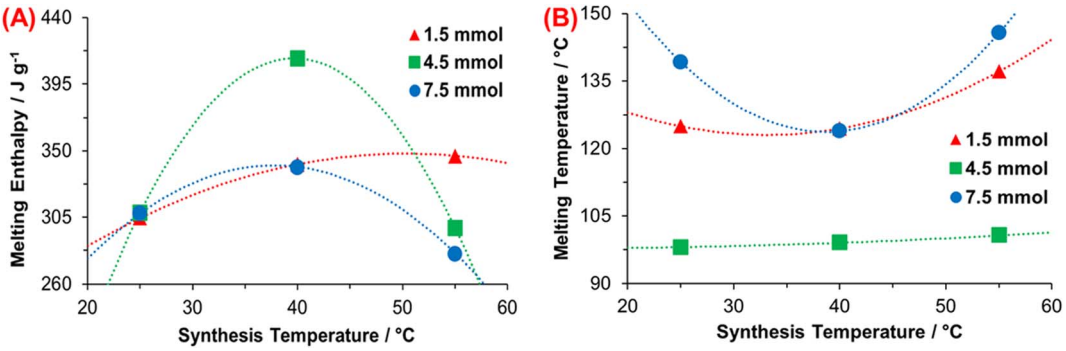

Fig. 9 Relationship between (A) rate constant and enthalpy of fusion, and (B) synthesis and melting temperature.

this also depends on crystallite defects or size. Results for 4.5 mmol TRIS show a minimum effect of the temperature on melting point; that means greater homogeneity of the crystalline regions or a reduced number of crystal defects. When the polymer is heated, the chains begin to move gradually as temperature increases and the crystalline domains are fused. The movement of chains depends on many aspects like main-chain symmetry and flexibility, polarity, tacticity, type/size of side-groups, and residual monomer/solvent.[65] As mentioned above, PDA is constituted by oligomers, which are made up of 2–8 monomers,[64,66] such as DHI and DA, in the beginning.

It is relevant due to the rigidity of the DHI compared to DA molecules; DHI has two aromatic rings, which reduce the flexibility, while the DA has a catechol moiety and an aliphatic branch which make its movement less restrictive. In the same way, oligomers with more monomers (*e.g.*, 8 DHI molecules) mean a more restricted motion than smaller oligomers (*e.g.*, 4 DHI). Results at 1.5 and 7.5 mmol show a considerable difference in melting temperatures, but with similar tendencies; this is ascribed to different ratios of DHI/DA monomers and polymerized degree of oligomers (2–8 units) derived from synthesis conditions.

3.5 Spectroscopic analysis

Infra-Red and Raman spectroscopies were carried out for the structural characterization to understand the effect of synthesis conditions on PDA and its influence on thermal properties. Fig. 10 illustrates the FTIR spectra of PDA obtained at 1.5, 4.5, and 7.5 mmol TRIS. Firstly, the broad peak between 3200–3700 cm^{-1} is associated with the tension of the O–H and N–H groups; O–H is related to the catechol moiety, while N–H is attributed to amine groups of 5,6-dihydroxyindole and dopamine molecules in the PDA structure.[35,40] Overlap vibrations of the benzene ring (C=C) and stretching vibrations of amine group bands are present at ~1573 cm^{-1}. Primary amines (N–H) have signals at 1550–1650 and 1050–1100 cm^{-1}, whereas secondary amines (C–N) are at 1500–1550 and 1100–1200 cm^{-1}. Different amines are related to the presence of DHI or DA molecules; DA has primary amines, while DHI has secondary amines. Bands between 1460 and 1340 cm^{-1} are attributed to the bending vibration of aliphatic groups (–CH_2–, C–H),[67,68] coming from the aliphatic branch of DA. Finally, stretching vibration of phenolic groups (C–OH) band is observed between 1230–1290 cm^{-1}.[69]

Table 5 lists the ratio between primary and secondary amine intensities.[70] A ratio below unity is observed for all materials; it specifies a higher quantity of secondary amine groups, indicating a conformation based mainly on DHI monomers. The 4.5 mmol TRIS concentration displays a high ratio of 1075/1150 cm^{-1}. A more subtle difference is observed in the 1600/1525 cm^{-1} ratio; it could be due to the overlapping bands from the benzene ring (C=C, 1560–1630 cm^{-1}) and amine groups. These results—in comparison with the other two concentrations—demonstrate a higher presence of DA monomers in PDA, which supports the DSC results where the aliphatic branch, that even having a 3-dimensional structure since it is aliphatic the primary bonds allows rotational movement, which needs less energy to begin to move compared to the aromatic structure of DHI, which is more voluminous and rigid.[71,72]

On the other hand, the higher presence of secondary amine in materials obtained at 1.5 and 7.5 mmol TRIS is associated with favoring DA cyclization (DHI monomers) and contributes

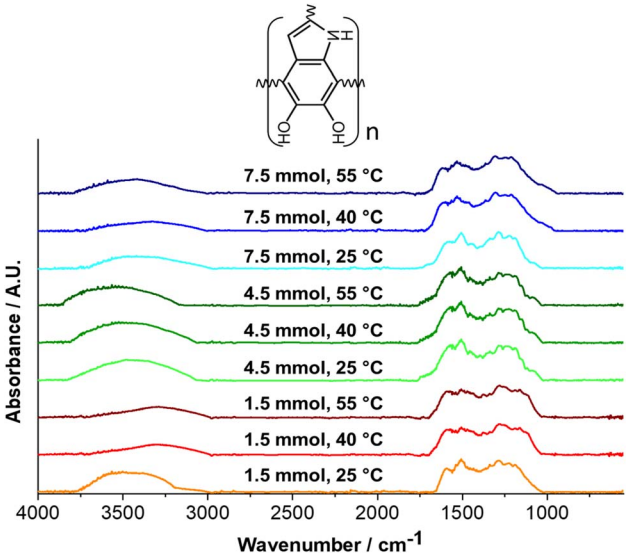

Fig. 10 FT-IR spectra of PDA at each synthesis condition from 550 to 4000 cm^{-1}.

Table 5 Intensities ratio of primary and secondary amine bands measured by FT-IR

Material		Intensity ratio (NH_2/NH)	
		1600/1525 cm^{-1}	1075/1150 cm^{-1}
1.5 mmol	25 °C	0.72	0.24
	40 °C	0.91	0.18
	55 °C	0.92	0.23
4.5 mmol	25 °C	0.85	0.31
	40 °C	0.87	0.32
	55 °C	0.86	0.30
7.5 mmol	25 °C	0.74	0.20
	40 °C	0.84	0.20
	55 °C	0.79	0.24

to a more rigid structure observed through the differences and higher values of melting temperatures—DSC results.

In addition, Fig. 11 displays the Raman spectra of synthesized PDA; two distinct bands, D (amorphous band—sp^3 and H) and G (graphitic band—sp^2), are shown in all samples. The first one, the D-band at ~1374 cm^{-1}, and the second one, the G-band at ~1579 cm^{-1}, originated from linear stretching of C–C bonds inside the rings and in-plane stretching of the aromatic rings,[59,73] respectively. The intensity ratio (I_D/I_G) is utilized to identify the degree of defects in a material where a low ratio indicates a low number of defects; consequently, the material presents a more graphitic structure with an sp^2 phase. The I_D/I_G ratio for 1.5 and 7.5 mmol TRIS displays similar values. These were below the unity that signifies the predominance of the graphite-like structure (sp^2 bonds) associated with the π–π stacking layers model as has been proposed for PDA; on the other hand, higher values of I_D/I_G ratio at 4.5 mmol reveal a lower graphite-like arrangement.

Notwithstanding, a specific analysis of the position of the G-band indicates a gradual blue shift (Fig. 12). According to Li, H. *et al.*,[57] the change of the G-band (to blue) is associated with carbonized PDA, where the amorphous carbon structure of PDA is converted to nanocrystalline graphite. The PDA synthesized here was not carbonized, but a relationship was established between the synthesis temperature and the blue shift, Fig. 12. We think that the synthesis temperature can also affect the PDA structure.

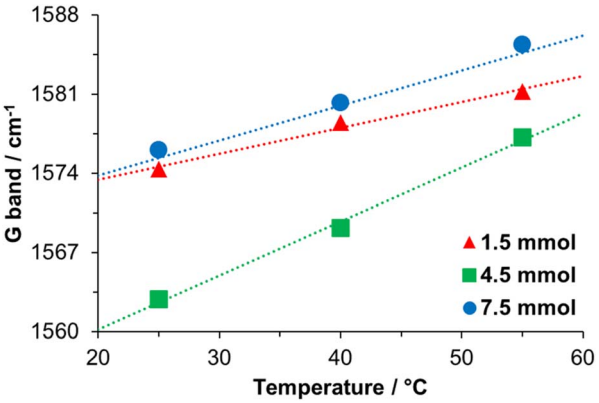

Fig. 12 Relationship between the temperature of the reaction and the G band position.

In particular, the low positions of the G-bands and the high I_D/I_G ratio for materials obtained at 4.5 mmol TRIS concentration compared with the other two concentrations could be explained due to the presence of DA monomers. Monomers constituted by DHI molecules are planar structures with π–π bonds (sp^2 hybridization), allowing monomers to stack in a graphitic-like structure. Nevertheless, when DA molecules form part of oligomers, the presence of π–π bonds is reduced, and sp^3 hybridization (characteristic hybridization of amorphous carbon material) increases.[74]

3.6 X-ray diffraction analysis

The X-ray diffraction analysis was used to carry out a microstructural analysis of PDA, see Fig. 13. PDA is a material composed of oligomers which in turn are mainly composed of DHI molecules that make up graphitic-like structures by π–π stacked. The peak center of XRD spectra is located between 21.6 and 23.4 (2θ), with variation in the distance of the layers

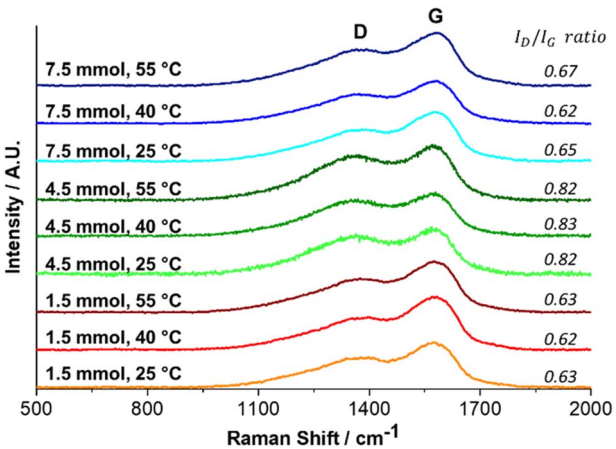

Fig. 11 Raman spectra of PDA at each synthesis condition.

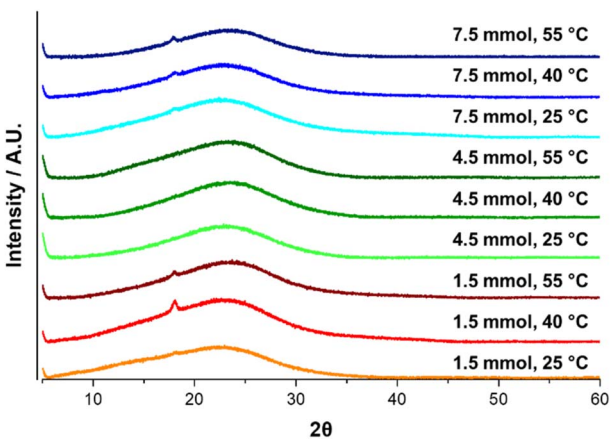

Fig. 13 X-ray diffraction spectra of PDA for each synthesis. condition.

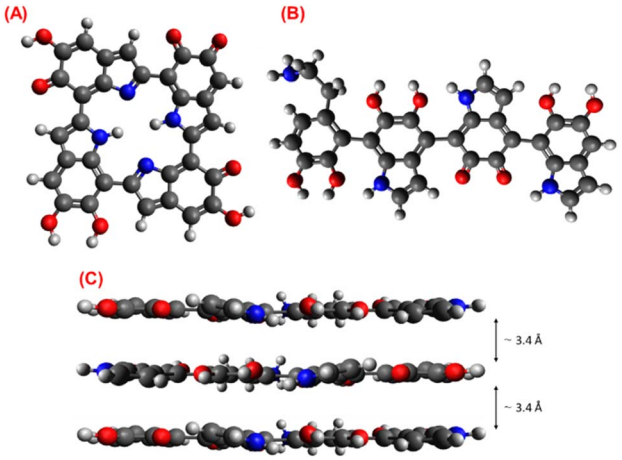

Fig. 14 Representation of monomer proposed by (A) Meng and Karixas, (B) Liebscher, and (C) three-layer stacked model for PDA. Atoms color: black, blue, red, and white for carbon, nitrogen, oxygen, and hydrogen, respectively.

between 3.4 and 4.1 Å, which could be mainly associated with the synthesis media molecules trapped between them.[58,66,75]

The center peak of PDA spectra for all materials was located at 23.1 ± 0.1 (2θ), which indicates a typical graphitic-like structure and suggests a *d*-spacing of ~3.4 Å. No effect from the synthesis conditions is observed for the XRD spectra; it can be associated with the reaction media since the water was used as the solvent.

Fig. 14 shows the two most used monomers to explain the PDA structure and its stacking as a graphitic-like structure. Fig. 14A presents an oligomer formed by four DHI molecules and its different oxidized forms; this cyclic model (Cyclotetramer) proposed by Meng and Karixas has been obtained through density functional theory (DFT) calculus, and despite explaining the optical absorption of natural melanin and PDA, it has not been experimentally proven.[76] On the other hand, Fig. 14B illustrates the PDA monomer structure based on spectroscopic and DFT results, the Liebscher model.[77] In this model, the composition of oligomers is formed by a mixture of DHI units with different unsaturation degrees (DHI and its oxidized forms) and open-chain dopamine units (DA) united covalently by carbon atoms in the 4 and 7 positions; results that support the presence of PDA chains of this kind also were reported by P. Delparastan *et al.*,[78] where also was identified the interaction between chains by reversible non-covalent interactions.

According to the results obtained from the thermal and spectroscopic analysis, the presence of DA units in the PDA chains has been inferred; consequently, the Liebscher model adjusts and describes the observed properties of the PDA. Finally, Fig. 14C shows the stacking structure of PDA chains with a *d*-spacing of ~3.4 Å supported by the π–π interactions.

4 Conclusions

The kinetics for most of the PDA synthesized using TRIS have been shown to have a conventional Arrhenius-type behavior. However, high TRIS concentrations have different implications as the inhibition/termination process affects the rate constant and the conversion yield.

The correlation between PDA morphology and TRIS concentration/temperature is well established in the literature. Nonetheless, this work has proven that morphology is mainly related to the rate constant, which depends on TRIS concentration and temperature but does not behave linearly concerning these conditions.

It has been identified that the ratio of primary and secondary amines in the PDA is essential to understanding its structure since the presence of primary amines—associated with DA monomers—affects it, as DSC thermograms and FT-IR spectra showed.

In this work, the existence of crystalline regions, within the PDA particles, was corroborated by DSC, Raman, and XRD analysis in contraposition to conventionally reported amorphous structure.

Author contributions

Alma Berenice Jasso-Salcedo. Data curation, formal analysis, writing-review & editing. Juan Carlos García-Mayorga. Data curation, formal analysis, methodology, investigation, writing-original draft. Haret-Codratian Rosu. Data curation, formal analysis, writing-review & editing. Vladimir A. Escobar-Barrios. Conceptualization, formal analysis, data curation, methodology, supervision, writing-review & editing.

Conflicts of interest

There are no conflicts to declare.

Acknowledgements

The authors acknowledge the technical support of MSc. Beatriz Escoto & Ana Iris Peña from LINAN (IPICYT) and Dr Pavel Hernández from LANOCAT (IPICYT).

References

1 F. Solano, Melanin and melanin-related polymers as materials with biomedical and biotechnological applications—Cuttlefish ink and mussel foot proteins as inspired biomolecules, *Int. J. Mol. Sci.*, 2017, **18**, 1561.
2 S. Ito and K. Wakamatsu, Quantitative Analysis of Eumelanin and Pheomelanin in Humans, Mice, and Other Animals: a Comparative Review, *Pigm. Cell Res.*, 2003, **16**, 523–531.
3 T. Ligonzo, *et al.*, Electrical and optical properties of natural and synthetic melanin biopolymer, *J. Non-Cryst. Solids*, 2009, **355**, 1221–1226.
4 M. Abbas, *et al.*, Structural, electrical, electronic and optical properties of melanin films, *Eur. Phys. J. E: Soft Matter Biol. Phys.*, 2009, **28**, 285–291.

5 A. Postma, *et al.*, Self-Polymerization of Dopamine as a Versatile and Robust Technique to Prepare Polymer Capsules, *Chem. Mater.*, 2009, **21**, 3042–3044.
6 Y. Liu, K. Ai and L. Lu, Polydopamine and Its Derivative Materials: Synthesis and Promising Applications in Energy, Environmental, and Biomedical Fields, *Chem. Rev.*, 2014, **114**, 5057–5115.
7 M. Ambrico, *et al.*, From commercial tyrosine polymers to a tailored polydopamine platform: concepts, issues and challenges en route to melanin-based bioelectronics, *J. Mater. Chem. C*, 2015, **3**, 6413–6423.
8 G. Siciliano, *et al.*, Polydopamine-Coated Magnetic Iron Oxide Nanoparticles: From Design to Applications, *Nanomaterials*, 2022, **12**, 1145.
9 X. Sun, L. Yan, R. Xu, M. Xu and Y. Zhu, Surface modification of TiO_2 with polydopamine and its effect on photocatalytic degradation mechanism, *Colloids Surf., A*, 2019, **570**, 199–209.
10 A. Mehdinia, S. Heydari and A. Jabbari, Synthesis and characterization of reduced graphene oxide-Fe_3O_4@polydopamine and application for adsorption of lead ions: Isotherm and kinetic studies, *Mater. Chem. Phys.*, 2020, **239**, 121964.
11 Y. Zou, *et al.*, Synthetic Melanin Hybrid Patchy Nanoparticle Photocatalysts, *J. Phys. Chem. C*, 2019, **123**, 5345–5352.
12 J. Dai, *et al.*, Surface modification of polypropylene with porous polyacrylamide/polydopamine composite coating, *Mater. Lett.*, 2020, **266**, 127487.
13 L. Jia, *et al.*, Polydopamine-assisted surface modification for orthopaedic implants, *J. Orthop. Transl.*, 2019, **17**, 82–95, DOI: 10.1016/j.jot.2019.04.001.
14 L. Migliaccio, M. Gryszel, V. Derek, A. Pezzella and E. D. Głowacki, Aqueous photo(electro)catalysis with eumelanin thin films, *Mater. Horiz.*, 2018, **5**, 984–990.
15 J. He, Y. Lu, T. Zhao and Y. Li, Preparation of polydopamine-coated, graphene oxide/Fe_3O_4-imprinted nanoparticles for selective removal of sulfonylurea herbicides in cereals, *J. Sci. Food Agric.*, 2020, **100**, 3822–3831.
16 H. Ma, *et al.*, Anchoring of Prussian blue nanoparticles on polydopamine nanospheres as an efficient peroxidase mimetic for colorimetric sensing, *Colloids Surf., A*, 2019, **577**, 622–629.
17 A. Sukeri, A. Arjunan and M. Bertotti, New strategy to fabricate a polydopamine functionalized self-supported nanoporous gold film electrode for electrochemical sensing applications, *Electrochem. Commun.*, 2020, **110**, 106622.
18 Z. Jin, *et al.*, Preparation of doxorubicin-loaded porous iron oxide@polydopamine nanocomposites for MR imaging and synergistic photothermal–chemotherapy of cancer, *Colloids Surf., B*, 2021, **208**, 112107.
19 L. Li, C. Xie and X. Xiao, Polydopamine modified TiO_2 nanotube arrays as a local drug delivery system for ibuprofen, *J. Drug Delivery Sci. Technol.*, 2020, **56**, 101537.
20 U. T. Uthappa, *et al.*, Facile green synthetic approach of bio inspired polydopamine coated diatoms as a drug vehicle for controlled drug release and active catalyst for dye degradation, *Microporous Mesoporous Mater.*, 2019, **288**, 109572.
21 X. Zhu, *et al.*, Core–shell structured Pd catalyst layer encapsulated by polydopamine for a gas–liquid–solid microreactor, *Appl. Surf. Sci.*, 2019, **487**, 416–425.
22 K. Zhu, *et al.*, Encapsulation of Fe_0-dominated Fe_3O_4/Fe_0/Fe_3C nanoparticles into carbonized polydopamine nanospheres for catalytic degradation of tetracycline *via* persulfate activation, *Chem. Eng. J.*, 2019, **372**, 304–311.
23 C. C. Ho and S. J. Ding, Structure, properties and applications of mussel-inspired polydopamine, *J. Biomed. Nanotechnol.*, 2014, **10**, 3063–3084.
24 M. Salomäki, L. Marttila, H. Kivelä, T. Ouvinen and J. Lukkari, Effects of pH and Oxidants on the First Steps of Polydopamine Formation: A Thermodynamic Approach, *J. Phys. Chem. B*, 2018, **122**, 6314–6327.
25 X. Wang, *et al.*, Size control synthesis of melanin-like polydopamine nanoparticles by tuning radicals, *Polym. Chem.*, 2019, **10**, 4194–4200.
26 M. Wu, T. Wang, L. Müller and F. A. Müller, Adjustable synthesis of polydopamine nanospheres and their nucleation and growth, *Colloids Surf., A*, 2020, **603**, 125196.
27 V. Ball, D. d. Frari, V. Toniazzo and D. Ruch, Kinetics of polydopamine film deposition as a function of pH and dopamine concentration: Insights in the polydopamine deposition mechanism, *J. Colloid Interface Sci.*, 2012, **386**, 366–372.
28 Y. Wang, *et al.*, Effects of Melanin on Optical Behavior of Polymer: From Natural Pigment to Materials Applications, *ACS Appl. Mater. Interfaces*, 2018, **10**, 13100–13106.
29 N. F. della Vecchia, *et al.*, Tris buffer modulates polydopamine growth, aggregation, and paramagnetic properties, *Langmuir*, 2014, **30**, 9811–9818.
30 F. Bernsmann, *et al.*, Dopamine-melanin film deposition depends on the used oxidant and buffer solution, *Langmuir*, 2011, **27**, 2819–2825.
31 C. C. Ho and S. J. Ding, The pH-controlled nanoparticles size of polydopamine for anti-cancer drug delivery, *J. Mater. Sci.: Mater. Med.*, 2013, **24**, 2381–2390.
32 N. F. della Vecchia, *et al.*, Building-block diversity in polydopamine underpins a multifunctional eumelanin-type platform tunable through a quinone control point, *Adv. Funct. Mater.*, 2013, **23**, 1331–1340.
33 M. Zhang, *et al.*, Precise synthesis of unique polydopamine/mesoporous calcium phosphate hollow Janus nanoparticles for imaging-guided chemo-photothermal synergistic therapy, *Chem. Sci.*, 2017, **8**, 8067–8077.
34 M. Mohammad, F. Ahmadpoor, S. A. Shojaosadati and E. Vasheghani-Farahani, Highly efficient porous magnetic polydopamine/copper phosphate with three-dimensional hierarchical nanoflower morphology as a selective platform for recombinant proteins separation, *Colloids Surf., B*, 2022, **209**, 112149.
35 A. S. Douglas, *Principios de Análisis Instrumental*, 2008.
36 J. D. Simon, Spectroscopic and dynamic studies of the epidermal chromophores trans-urocanic acid and eumelanin, *Acc. Chem. Res.*, 2000, **33**, 307–313.

37 R. Micillo, *et al.*, Eumelanin broadband absorption develops from aggregation-modulated chromophore interactions under structural and redox control, *Sci. Rep.*, 2017, **7**, 41532.
38 A. Solís-Herrera, C. María del Carmen Arias Esparza, R. I. Solís-Arias, P. E. Solís-Arias and M. P. Solís-Arias, The physical and chemical properties of eumelanin, *Biomed. Res.*, 2010, **21**, 224–226.
39 R. Lakshminarayanan, S. Madhavi and C. P. C. Sim, Oxidative Polymerization of Dopamine: A High-Definition Multifunctional Coatings for Electrospun Nanofibers – An Overview. in *Dopamine Health and Disease*, InTech, 2018, DOI: **10.5772/intechopen.81036**.
40 C. C. Ho and S. J. Ding, Structure, properties and applications of mussel-inspired polydopamine, *J. Biomed. Nanotechnol.*, 2014, **10**, 3063–3084, DOI: **10.1166/jbn.2014.1888**.
41 S. Hong, *et al.*, Non-covalent self-assembly and covalent polymerization co-contribute to polydopamine formation, *Adv. Funct. Mater.*, 2012, **22**, 4711–4717.
42 J. Liebscher, Chemistry of Polydopamine – Scope, Variation, and Limitation, *Eur. J. Org. Chem.*, 2019, **2019**, 4976–4994, DOI: **10.1002/ejoc.201900445**.
43 M. D'Ischia, A. Napolitano, V. Ball, C. T. Chen and M. J. Buehler, Polydopamine and eumelanin: from structure–property relationships to a unified tailoring strategy, *Acc. Chem. Res.*, 2014, **47**, 3541–3550.
44 N. Ira, *Levine. Principios de fisicoquímica.*, Mc Graw Hill, 2014.
45 C. Zhao, *et al.*, Mussel-inspired one-pot synthesis of a fluorescent and water-soluble polydopamine-polyethyleneimine copolymer, *Macromol. Rapid Commun.*, 2015, **36**, 909–915.
46 Z. Wang, *et al.*, Tunable, Metal-Loaded Polydopamine Nanoparticles Analyzed by Magnetometry, *Chem. Mater.*, 2017, **29**, 8195–8201.
47 K. Y. Ju, Y. Lee, S. Lee, S. B. Park and J. K. Lee, Bioinspired polymerization of dopamine to generate melanin-like nanoparticles having an excellent free-radical-scavenging property, *Biomacromolecules*, 2011, **12**, 625–632.
48 S. U. Triyono, Correlation between pre-exponential factor and activation energy of isoamyl alcohol hydrogenolysis on platinum catalysts, *Indones. J. Chem.*, 2004, **4**, 1–5.
49 N. Katada, S. Sota, N. Morishita, K. Okumura and M. Niwa, Relationship between activation energy and pre-exponential factor normalized by the number of Brønsted acid sites in cracking of short chain alkanes on zeolites, *Catal. Sci. Technol.*, 2015, **5**, 1864–1869.
50 S. G. Kwon and T. Hyeon, Formation mechanisms of uniform nanocrystals *via* hot-injection and heat-up methods, *Small*, 2011, **7**, 2685–2702, DOI: **10.1002/smll.201002022**.
51 V. K. Thakur, M. F. Lin, E. J. Tan and P. S. Lee, Green aqueous modification of fluoropolymers for energy storage applications, *J. Mater. Chem.*, 2012, **22**, 5951–5959.
52 J. Ribera, *et al.*, Scalable Biosynthesis of Melanin by the Basidiomycete Armillaria cepistipes, *J. Agric. Food Chem.*, 2019, **67**, 132–139.
53 A. M. Gómez-Marín and C. I. Sánchez, Thermal and mass spectroscopic characterization of a sulphur-containing bacterial melanin from *Bacillus subtilis*, *J. Non-Cryst. Solids*, 2010, **356**, 1576–1580.
54 B. Tawiah, B. Yu, A. C. Y. Yuen and B. Fei, Facile preparation of uniform polydopamine particles and its application as an environmentally friendly flame retardant for biodegradable polylactic acid, *J. Fire Sci.*, 2020, **38**, 485–503.
55 K. Shanmuganathan, J. H. Cho, P. Iyer, S. Baranowitz and C. J. Ellison, Thermooxidative stabilization of polymers using natural and synthetic melanins, *Macromolecules*, 2011, **44**, 9499–9507.
56 A. P. Tiwari, *et al.*, Polydopamine-based Implantable Multifunctional Nanocarpet for Highly Efficient Photothermal-chemo Therapy, *Sci. Rep.*, 2019, **9**, 2943.
57 H. Li, *et al.*, Structure Evolution and Thermoelectric Properties of Carbonized Polydopamine Thin Films, *ACS Appl. Mater. Interfaces*, 2017, **9**, 6655–6660.
58 E. Coy, I. Iatsunskyi, J. C. Colmenares, Y. Kim and R. Mrówczyński, Polydopamine Films with 2D-like Layered Structure and High Mechanical Resilience, *ACS Appl. Mater. Interfaces*, 2021, **13**, 23113–23120.
59 Y. Kim and J. Kim, Carbonization of polydopamine-coating layers on boron nitride for thermal conductivity enhancement in hybrid polyvinyl alcohol (PVA) composites, *Polymers*, 2020, **12**, 1410.
60 F. J. Lanyi, N. Wenzke, J. Kaschta and D. W. Schubert, On the Determination of the Enthalpy of Fusion of α-Crystalline Isotactic Polypropylene Using Differential Scanning Calorimetry, X-Ray Diffraction, and Fourier-Transform Infrared Spectroscopy: An Old Story Revisited, *Adv. Eng. Mater.*, 2020, **22**, 1900796.
61 Y. Kong and J. N. Hay, The enthalpy of fusion and degree of crystallinity of polymers as measured by DSC, *Eur. Polym. J.*, 2003, **39**, 1721–1727.
62 P. K. Gallagher, *Handbook of thermal analysis and calorimetry, vol. 3*, ELSEVIER, 2002.
63 B. Simonovic, *et al.*, Thermogravimetry and differential scanning calorimetry of natural and synthetic melanins, *J. Therm. Anal.*, 1990, **36**, 2475–2482.
64 X. Yu, H. Fan, Y. Liu, Z. Shi and Z. Jin, Characterization of carbonized polydopamine nanoparticles suggests ordered supramolecular structure of polydopamine, *Langmuir*, 2014, **30**, 5497–5505.
65 W. Groenewoud, *Characterisation of polymers by thermal analysis*, ELSEVIER, 2001.
66 D. R. Dreyer, D. J. Miller, B. D. Freeman, D. R. Paul and C. W. Bielawski, Elucidating the structure of poly(dopamine), *Langmuir*, 2012, **28**, 6428–6435.
67 I. E. Pralea, *et al.*, From extraction to advanced analytical methods: the challenges of melanin analysis, *Int. J. Mol. Sci.*, 2019, **20**, 3943.
68 L. F. Wang and J. W. Rhim, Isolation and characterization of melanin from black garlic and sepia ink, *LWT–Food Sci. Technol.*, 2019, **99**, 17–23.
69 C. Marín-Sanhueza, *et al.*, Stress Dependent Biofilm Formation and Bioactive Melanin Pigment Production by

a Thermophilic *Bacillus* Species from Chilean Hot Spring, *Polymers*, 2022, **14**, 680.

70 V. A. Escobar Barrios, J. R. Rangel Méndez, N. V. Pérez Aguilar, G. A. Espinosa and J. L. Dávila Rodríguez, FTIR-An Essential Characterization Technique for Polymeric Materials, *Infrared Spectroscopy*, 2012, pp. 195–212.

71 J. M. G. Cowie and V. Arrighi, *Polymers: Chemistry and Physics of Modern Materials*, CRC Press, 2007.

72 J. C. Markwart, *et al.*, Aromatic *vs.* aliphatic hyperbranched polyphosphoesters as flame retardants in epoxy resins, *Molecules*, 2019, **24**, 3901.

73 T. Wang, M. Xia and X. Kong, The pros and cons of polydopamine-sensitized titanium oxide for the photoreduction of CO_2, *Catalysts*, 2018, **8**, 2015.

74 A. C. Ferrari and J. Robertson, Interpretation of Raman spectra of disordered and amorphous carbon, *Phys. Rev. B: Condens. Matter Mater. Phys.*, 2000, 14095–14107, DOI: 10.1103/PhysRevB.61.14095.

75 H. Fan, *et al.*, Folic acid-polydopamine nanofibers show enhanced ordered-stacking *via* π–π interactions, *Soft Matter*, 2015, **11**, 4621–4629.

76 S. Meng and E. Kaxiras, Theoretical models of eumelanin protomolecules and their optical properties, *Biophys. J.*, 2008, **94**, 2095–2105.

77 J. Liebscher, *et al.*, Structure of polydopamine: a never-ending story?, *Langmuir*, 2013, **29**, 10539–10548.

78 P. Delparastan, K. G. Malollari, H. Lee and P. B. Messersmith, Direct Evidence for the Polymeric Nature of Polydopamine, *Angew. Chem., Int. Ed.*, 2019, **58**, 1077–1082.